Charge Separation Enhancement Enables Record Photocurrent Density in Cu2ZnSn(S,Se)(4) Photocathodes for Efficient Solar Hydrogen Production

Guangxing Liang, Zhidong Li, Muhammad Ishaq, Zhuanghao Zheng, Zhenghua Su, Hongli Ma, Xianghua Zhang, Ping Fan, Shuo Chen

▶ **To cite this version:**

Guangxing Liang, Zhidong Li, Muhammad Ishaq, Zhuanghao Zheng, Zhenghua Su, et al.. Charge Separation Enhancement Enables Record Photocurrent Density in Cu2ZnSn(S,Se)(4) Photocathodes for Efficient Solar Hydrogen Production. Advanced Energy Materials, 2023, pp.2300215. 10.1002/aenm.202300215 . hal-04057525

HAL Id: hal-04057525
https://hal.science/hal-04057525v1

Submitted on 11 Sep 2024

HAL is a multi-disciplinary open access archive for the deposit and dissemination of scientific research documents, whether they are published or not. The documents may come from teaching and research institutions in France or abroad, or from public or private research centers.

L'archive ouverte pluridisciplinaire **HAL**, est destinée au dépôt et à la diffusion de documents scientifiques de niveau recherche, publiés ou non, émanant des établissements d'enseignement et de recherche français ou étrangers, des laboratoires publics ou privés.

Revised Manuscript

Charge Separation Enhancement Enables Record Photocurrent Density in $Cu_2ZnSn(S,Se)_4$ Photocathodes for Efficient Solar Hydrogen Production

*Guangxing Liang, Zhidong Li, Muhammad Ishaq, Zhuanghao Zheng, Zhenghua Su, Hongli Ma, Xianghua Zhang, Ping Fan, and Shuo Chen**

G. Liang, Z. Li, M. Ishaq, Z. Zheng, Z. Su, P. Fan, S. Chen
Shenzhen Key Laboratory of Advanced Thin Films and Applications, Key Laboratory of Optoelectronic Devices and Systems of Ministry of Education and Guangdong Province, College of Physics and Optoelectronic Engineering
Shenzhen University
Shenzhen, Guangdong 518060, China
E-mail: chensh@szu.edu.cn (S. Chen)
H. Ma, X. Zhang
CNRS, ISCR (Institut des Sciences Chimiques de Rennes), UMR 6226
Université de Rennes
Rennes F-35000, France

Keywords: $Cu_2ZnSn(S,Se)_4$; Photocathode; Charge separation; Photocurrent density; Solar hydrogen production

Abstract: $Cu_2ZnSn(S,Se)_4$ (CZTSSe) is a promising light absorbing semiconductor for solar energy conversion in photovoltaic cells and photo-electrochemical (PEC) water-splitting devices, owing to its earth-abundant constituents, adjustable band-gap and superior absorption coefficient. However, the severe charge carrier recombination and the sluggish charge separation efficiency have been the main issues obstructing the enhancement of device performance. In this work, a planar-type Mo/CZTSSe/CdS/TiO_2/Pt photocathode is fabricated. High-quality CZTSSe film with compact and uniform crystal grains can be obtained via a two-step process involving solution processed spin coating and thermally processed selenization. Under an appropriate film thickness, both bulk defects and surface/interface defects are passivated, significantly suppressing the defects-

assisted recombination. Moreover, the benign energy band alignment of CZTSSe/CdS heterojunction is favorable to enhance photo-generated charge separation and transfer efficiency. Finally, a remarkable photocurrent density of 40.40 mA/cm^2 (at 0 V_{RHE}) can be achieved, approaching to its theoretical value of 42.85 mA/cm^2, and representing the highest value reported to date for kesterites-based photocathodes. A champion CZTSSe photocathode with stimulating half-cell solar-to-hydrogen conversion efficiency of 6.47% undoubtedly paves a bright avenue for its efficient solar hydrogen production applications.

1. Introduction

Hydrogen energy is an attractive carbon-free energy source that can be utilized in multiple energy fields including industry, transportation, and heating.[1] However, most hydrogen is presently produced by the burning of fossil fuels, accompanied with severe carbon emission issues. Harvesting sunlight to produce green hydrogen energy is a potential strategy for overcoming the energy shortage and the global environmental crisis, though it still remains challenging.[2] Since the discovery of photoelectrochemical (PEC) water splitting, continuous efforts have been dedicated to develop PEC photoelectrodes for efficient solar hydrogen production via water splitting.[3-5] Some well-researched oxides, e.g., Cu_2O[6], $CuFeO_2$,[7] and chalcogenides such as $CuGaSe_2$,[8] $CuInS_2$[9,10] and $CuIn_{1-x}Ga_xSe_2$ (CIGS),[11,12,13] as well as newly emerging $Cu_2BaSn(S,Se)_4$,[14] Cu_2ZnSnS_4 (CZTS)[15] and Sb_2Se_3[16,17] are explored as photoanode or photocathode materials. It should be mentioned that the CIGS-based thin-film photocathode has achieved a record half-cell solar-to-hydrogen (HC-STH) conversion efficiency of 9.3%,[11] accompanied with photocurrent density (J_{ph}) of 35.5 mA/cm^2 at 0 V versus reversible hydrogen electrode (RHE).[12] However, the use of earth's scarce elements like indium (In) and

gallium (Ga) is a substantial large-scale application limitation for CIGS-based photocathodes. To overcome this shortage, earth-abundant, cost-effective and environmentally benign kesterites (e.g., CZTS) have drawn much attention as a potential alternative to its cousin chalcopyrite CIGS in photoelectric application scenarios, including PEC water splitting.[18] For instance, Jiang et al. reported that a spray-sulfurized CZTS absorber layer coupled with sandwich structured buffer layer of HfO_2/CdS/HfO_2 could achieve an appreciable J_{ph} of 28 mA/cm^2 at 0 V_{RHE}, onset potential (V_{on}) of 0.72 V_{RHE}, and therefore interesting HC-STH conversion efficiency of 7.27%.[15] Notably, the theoretical J_{ph} of CZTS photocathode might be limited by its intrinsic absorption wavelength range with an assumption of 100% incident photon-to-current conversion efficiency. By contrast, quasi-direct band-gap of quinary compound $Cu_2ZnSn(S,Se)_4$ (CZTSSe) can be tuned over a desirable band-gap range of 1.5-1.0 eV, broadening light absorption wavelength range by gradually decreasing the sulfur to selenium ratio. Meanwhile, CZTSSe is conducive to light harvesting because of its much superior absorption coefficient (>10^4 cm^{-1}), leading to greater theoretical J_{ph} value.[19] Up to now, the investigation of CZTSSe-based photocathodes for PEC water splitting is relatively scarce. Thus, it is urgently warranted to prepare high-quality CZTSSe thin films and further to explore their application feasibility as efficient photocathodes in solar hydrogen production scenarios.

Solution-based approaches have been widely developed for preparing CZTSSe light absorbing films. These processes possess advantages of low cost, simple experimental instruments, effectively tunable chemical composition, and positively suppressed formation of secondary phases.[20] Various organic solvents, such as hydrazine,[21] dimethylsulfoxide (DMSO),[22,23] dimethylformamide

(DMF)[24] and 2-methoxyethanol (2-ME)[25] were explored and demonstrated effectiveness. Further comparison, hydrazine pure-solution assisted CZTSSe films are normally dense and large-grained. However, the detrimental micro-voids that exist at the CZTSSe-metal back contact interface, as well as the intrinsic toxic, inflammable and explosive characters of hydrazine might limit its large-scale commercial applications. DMSO-based CZTSSe precursors are not stable, leading to the as-fabricated film displays a clear bilayer feature with fine grains at bottom and large grains on top, which might hinder carrier transport across the absorber layer. DMF is a kind of aprotic solvent with better solubility and stability than DMSO, it can obtain large-grained CZTSSe absorber layer, though the severe interface contact issues remain an obstacle in the corresponding devices. Recently, our group demonstrated that 2-ME is a promising green organic solvent, a uniform and compact CZTSSe thin film can be fulfilled by adjusting key ratio of Sn^{4+} to Sn^{2+} in 2-ME based CZTS precursor solution, following an optimized selenization process, which is beneficial to enhance charge transfer and reduce current leakage.[25] Furthermore, combining some suitable cation doping, the concentration of some detrimental defects (e.g., Cu_{Zn}, Cu_{Sn} antisite defects, and $[2Cu_{Zn}+Sn_{Zn}]$ defect clusters) can be significantly suppressed, leading to interesting photovoltaic device efficiency exceeding 12%,[26] which can provide essential guidance for the fabrication of efficient CZTSSe photocathodes regarding similar device configuration.

In this work, a mild 2-ME organic solvent system was used to prepare CZTS precursor, followed by an additional thermodynamic/kinetic selenization treatment to obtain CZTSSe thin film. Introducing CdS as buffer layer, TiO_2 as protective layer, and Pt as co-catalyst, Mo/CZTSSe/CdS/TiO_2/Pt planar-type photocathode

was then fabricated. The CZTSSe light absorbing thin film has been demonstrated to remarkably contribute to the PEC performance of device. High-quality CZTSSe can be obtained under an optimal thickness, wherein, both bulk defects and interface defects can be suppressed as well as the defects-assisted recombination. Moreover, superior charge transfer efficiency and separation efficiency can be simultaneously realized, resulting in a highly interesting J_{ph} of 40.40 mA/cm^2 (at 0 V_{RHE}) that is close to its theoretical value. Therefore, the champion CZTSSe thin-film photocathode delivers stimulating HC-STH conversion efficiency of 6.47%, demonstrating high potential of solar hydrogen production applications.

2. Results and Discussion

Figure 1a illustrates the PEC performance characterizations of the Mo/CZTSSe/CdS/TiO_2/Pt photocathodes using electrochemical workstation. The applied potential ($V_{Ag/AgCl}$) can be transformed into V_{RHE} through Nernst Equation:[15]

$$V_{RHE} = V_{Ag/AgCl} + 0.059 \times \mathrm{PH} + 0.199 \quad (1)$$

while HC-STH conversion efficiency was calculated by the equation below:[27]

$$HC-STH\ (\%) = J_{ph} \times (V_{RHE} - V_{H^+/H_2})/P_{sun} \times 100\% \quad (2)$$

where V_{H^+/H_2} is the reduction potential for hydrogen (0 V_{RHE}), V_{RHE} is the potential relative to RHE, and P_{sun} is the AM 1.5G simulated sunlight intensity (100 mW/cm^2). Visible hydrogen bubbles produced and moved from photocathode surface to the electrolyte under illumination is shown in Figure 1b, indicating an effective Hydrogen Evolution Reaction (HER). A video of the real-time working model is also given in the Movie S1 (Supporting Information-Video). Moreover, the as-fabricated photocathode is quasi-homogeneous in appearance under device area over 16 cm^2 (Figure 1c), indicating its scalability in practical application scenarios. Generally, the light absorbing thin film thickness plays an important role in balancing charge carrier

generation and transport. Herein, CZTSSe thin films with different thicknesses were prepared and investigated, i.e., CZTSSe-1 of 8 spin coating cycles, CZTSSe-2 of 10 cycles, and CZTSSe-3 of 12 cycles, and the corresponding Mo/CZTSSe/CdS/TiO_2/Pt thin-film photocathodes were labeled as PC-1, PC-2, and PC-3, respectively. The chopped light dependent photocurrent density-potential (*J-V*) curves based on these photocathodes are shown in Figure 1d. To be specific, the J_{ph} values at 0 V_{RHE} are determined to 24.52 mA/cm^2, 40.40 mA/cm^2, and 30.31 mA/cm^2 in sequence. It is worth to mention that the obtained J_{ph} value of device PC-2 is significantly higher than that of previously reported kesterites (i.e., including CZTS, CZTSe and CZTSSe) thin-film photocathodes, also representing the top value for state-of-the-art chalcogenide-based photocathodes (Figure 1g and Table S1).[3,5,10,11,14,15,28-32] *J-V* curves associated to these devices in dark and continuous simulated sunlight irradiation are showed in Figure 1e, presenting a synchronous variation with strong correlation with CZTSSe film thickness. Additionally, Figure 1f exhibits the as-calculated HC-STH conversion efficiencies. The HC-STH peak value of device PC-2 is located in a more positive potential of 0.25 V_{RHE} as compared to that of device PC-1 (0.22 V_{RHE}) and PC-3 (0.22 V_{RHE}), indicating simultaneous upgradation in photocurrent and photovoltage, and thereby PEC performance.[5] Significantly, a stimulating 6.47% HC-STH conversion efficiency is also comparable to the current record value of 7.27% for CZTS-based photocathode (Figure 1h). The chopped photocurrent density-time (*J-T*) curves recorded under AM 1.5G sunlight irradiation exhibit similar J_{ph} variation upon CZTSSe film thickness, demonstrating excellent reversibility and stability (Figure S1a-c, Supporting Information). Moreover, the champion PC-2 device maintains ~90% of its initial J_{ph} after operation for 60 min at 0 V_{RHE} (Figure S1d), and even shows hydrogen production validity after 6 hous working (Movie S1), further strengthening its long-term stability.

To verify the key CZTSSe light absorbing thin film quality as well as its effect on device PEC performance, a systematical morphological and structural analysis was performed. **Figure 2**a shows the X-ray diffraction (XRD) patterns of CZTSSe at different film thicknesses. The presence of three major diffraction peaks of (112), (204), and (312), and the absence of any observable peaks out of standard kesterite CZTS (JCPDS Card No.52-0868) or CZTSe (JCPDS Card No. 26-0575) pattern validate the high crystallinity and purity of as-prepared CZTSSe thin films.[33,34] By contrast, the smaller FWHM (Full width at half maxima) values of diffraction peaks indicate larger crystal grains in CZTSSe-2 thin film (Figure 2b). Further analysis of Raman spectra confirm the absence of secondary phases. As shown in Figure 2c, significant primary peaks at 207 cm^{-1} can be assigned to the A1 vibration mode of CZTSe, which is caused by the vibration of selenium atoms within the lattice. Similarly, the 330 cm^{-1} Raman peak can be attributed to CZTS A vibration mode, which primarily derives from the vibration of sulfur atom. Such bimodal vibration modes match well with characteristics of $Cu_2ZnSn(S,Se)_4$ alloy,[27] and it can also be confirmed by typical XPS characterizations, with obvious Cu 2p, Zn 2p3, Sn 3d5, S 2p and Se 3d peaks in those three CZTSSe samples (Figure S2). The surface scanning electron microscopy (SEM) pictures of the CZTSSe are shown in Figure 2d-f. Wherein, the thinner CZTSSe-1 thin film is composed of mostly small crystals, accompanied with obvious micro-voids on the surface. In contrast, a more dense and large-grained thin film can be gained with increasing the thickness, which is closely related to its efficient thermodynamic/kinetic growth under sufficient temperature and Se atmosphere. The cross-sectional SEM images confirm this evolution (Figure 2h-i), and the specific absorber layer thicknesses are determined to 1.392 μm, 1.630 μm, and 1.958 μm for CZTSSe-1, CZTSSe-2, and CZTSSe-3, respectively. Obviously, for the CZTSSe-1 and CZTSSe-3 thin films, there are many cracks and/or micro-voids between large grains at top and fine grains at bottom, which might result in severe recombination of photon-generated carriers and current leakage. Significantly, highly compact and quasi-uniform CZTSSe thin film can be observed in

the well-adherent layer structured PC-2 thin-film photocathode. A visible $MoSe_2$ interfacial layer is resonably emerged due to the reaction of Mo substrate and Se vapor at adequate temperature. It has previously reported that the $MoSe_2$ layer with appropriate thickness is beneficial to reduce back contact barrier and accelerate charge carrier transfer.[5] Overall, the optimized CZTSSe-2 film with suitable thickness, large compact crystals, and benign interface is favorable for light absorption, charge carrier generation, separation and transport, and therefore higher PEC performance.

The energy band-gap (E_g) of CZTSSe was obtained through the reflection spectra, as shown in **Figure 3**a, covering wavelength from 300 nm to 1500 nm by using glass as substrate, and then calculated E_g value according to the following equations:[36]

$$2\alpha d = ln[(R_{max} - R_{min})/(R - R_{min})] \quad (3)$$

$$\alpha hv = C(hv - E_g)^n \quad (4)$$

where d is thin film thickness, R_{max} and R_{min} correspond to the critical reflectivity out and in light absorption region, α is the absorption coefficient, hv is energy of photon, C is a constant, n is an index as specified to 0.5 for direct band-gap semiconductor. The CZTSSe thin films with different thicknesses exhibit a quite similar E_g value of 1.06 eV (Figure 3b), fall in between CZTSe (i.e., 1.0 eV in theory) and CZTS (i.e., 1.5 eV in theory), indicating high composition-dependent adjustability and microstructure-dependent tolerance of band structure. Such an ideal narrow band-gap can also promote efficient sunlight harvesting. The theoretical photocurrent density of CZTSSe can be calculated through the AM 1.5G standard solar spectrum and wavelength-dependent light harvesting efficiency (LHE, Figure 3c) in term of the following formulas:[37]

$$J_{abs} = \int_{300}^{\lambda_e} \frac{\lambda}{1240} \cdot N_{ph}(\lambda) \cdot LHE(\lambda) d\lambda \quad (5)$$

$$\text{LHE} = 1 - 10^{-A(\lambda)} \quad (6)$$

where J_{abs} is the theoretical photocurrent density, λ_e is the absorption cut-off wavelength that is related to band-gap, λ is the wavelength, N_{ph} (λ) is the photo flux (Figure 3d), A (λ) is the absorbance related to wavelength (Figure S3). The λ_e is about 1170 nm, giving the J_{abs} of 42.85 mA/cm^2 for CZTSSe-2 (Figure 3d), and J_{abs} values of 34.80 mA/cm^2 and 38.61 mA/cm^2 for CZTSSe-1 and CZTSSe-3, respectively (Figure S3). Moreover, the transient photocurrent attenuation spectra of the photocathodes are displayed in Figure 3e, hence, the charge transfer efficiency (η_{tran}) can be obtained through the measured photocurrents associated to "light off" state and "light on" state,[38] since the electrode/electrolyte interface can temporarily accumulate charges. The charge separation efficiency (η_{sep}) can be further examined:[39]

$$\eta_{tran} = \frac{J_{ss}}{J_{inst}} \tag{7}$$

$$J_{ph} = J_{abs} \times \eta_{tran} \times \eta_{sep} \tag{8}$$

where J_{ss} is the steady state photocurrent density, and J_{inst} signifies the instantaneous photocurrent density. Accordingly, high η_{tran} values of 95.35%, 99.20% and 97.14% can be determined for PC-1, PC-2, and PC-3 devices, respectively, indicating functional electron transport layer to accelerate the photoelectron move from photocathode bulk to the electrode/electrolyte interface. In contrast, the calculated η_{sep} values are 73.05%, 95.04% and 80.81%, respectively. It is consistent with the aforementioned analysis of effect of absorber layer on charge carrier separation and transport, which is closely related to the CZTSSe thin film quality and CZTSSe/CdS heterojunction character. Then, time-resolved photoluminescence (TRPL) was introduced to examine minority carrier lifetimes of the CZTSSe thin films, as shown in Figure 3f, the obtained τ_1, τ_2 and τ_3 values associated to CZTSSe-1, CZTSSe-2, CZTSSe-3 thin films are 0.54 ns, 0.87 ns and 0.69 ns, respectively.[40] The minority

carrier (electrons) with longer lifetime (i.e. τ_2 in CZTSSe-2) undoubtedly possesses a higher probability to migrate to the electrode/electrolyte interface for HER occurring. The charge transfer kinetics were further investigated via electrochemical impedance test. Figure 3g-i shows the photoelectrochemical impedance spectroscopy (PEIS) analysis of the CZTSSe-based photocathodes under illumination. In general, the PEIS derived high-frequency arc (10^3~10^5 Hz) is affected by the bulk semiconductor capacitance (C_{HF}) and the charge transfer resistance inside the photoelectrode (R_{HF}), the middle-frequency arc (10^1~10^3 Hz) reflects the capacitance (C_{MF}) and the resistance (R_{MF}) of charge capture under surface trap states in the band-gap, and the low-frequency arc (10^{-1}~10^1 Hz) represents the capacitance of the electrode/electrolyte interface (C_{LF}) and the resistance of electrochemical charge-transfer reactions (R_{LF}, e.g., HER).[2] Nyquist plots with two arcs can be observed for all those three photocathodes, which are consistent with the corresponding bodes diagrams that comprise two regions covering frequency from 10 Hz to 100 kHz. Herein, the low-frequency dependent resistor–capacitor (R_{LF}-C_{LF}) component cannot be obviously observed since the existence of high concentration oxidizing substances (hydrogen ions) on the electrode surface and electrolyte, thus, it can assume that all the photoelectrons transferred to the electrode/electrolyte interface would generate hydrogen, i.e., the Faraday efficiency is 100%. An equivalent circuit system containing a series resistance (R_S) and two pairs of parallel resistor–capacitor (R-C) elements was used to fit the PEIS data. To be specific, the R_S can be attributed to the resistance of Mo/CZTSSe back contact interface, C_{HF} and R_{HF} represent the capacitance inside the space charge region of the CZTSSe/CdS heterojunction interface, and the corresponding charge transport resistance, while C_{MF} and R_{MF} signify the CZTSSe internal defect capacitance and resistance, respectively. The

fitted results are shown in Table S2. Quite similar and tolerable R_S values (~ 6.5-7.0 Ω) indicates a benign back contact interface, especially with appropriate $MoSe_2$ interfacial layer to improve carrier transport and reduce recombination. Considering the dominant role of capacitance at high frequency (Figure S4), the remarkably smaller C_{HF} value of device PC-2 (5.35×10^{-7} F) implies a shorter time for charge accumulation, a much smaller R_{HF} value also suggests more effective carrier separation and transport at the interface. In parallel, according to an ideal relationship between impedance and frequency at middle or low frequency, a much smaller R_{MF} value of 4.13 Ω indicates less bulk defects inside CZTSSe-2 absorber thin film, echoing the SEM results analysis.

Transmission electron microscope (TEM) characterization was then carried out to investigate the microstructure of Mo/CZTSSe/CdS/TiO_2/Pt photocathode. The cross-sectional TEM image distinctly exhibits its layered structure with clear CZTSSe/CdS and CdS/TiO_2 interfaces (**Figure 4**a). An ALD-grown TiO_2 layer with thickness of 10 nm can be observed at the top side, the lattice stripe with interplanar d-spacing of about 2.653 Å matches the distance of (101) lattice plane of TiO_2 (PDF No. 21-1276) (Figure 4c). Its proper crystallization in anatase phase is thermodynamically stable in aqueous electrolyte, which can prevent electrolyte permeation and protect the electrode from being photocorrosion. As shown in Figure 4d and 4e, according to the high-resolution transmission electron microscopy (HRTEM) images, the obtained interplanar d-spacing of 2.752 Å can be ascribed to (200) plane of CZTSSe, while the 2.822 Å lattice fringe matches well with (200) plane of CdS. Thus, CZTSSe/CdS heterojunction interface displays consecutive, well-adherent and superior lattice-matched characters, which is expected to suppress charge carrier recombination and facilitate charge carrier transport at interface. HRTEM image along with its derived selected area electron diffraction (SAED)

pattern further illustrates high crystallinity and typical kesterite crystal structure for the as-prepared CZTSSe (Figure 4f and 4g). Finally, TEM-coupled EDS element mapping and line scanning results show the rational chemical elements distribution in each functional layer (Figure S5). In addition, Kelvin probe force microscopy (KPFM) characterization was conducted to investigate the surface topography and surface potential of the optimized CZTSSe-2 thin film (Figure 4h and 4i). The surface topography is quite similar to that of surface SEM image, exhibiting large compact crystals (Figure 4h). The three dimensional (3D) potential mapping (inset in Figure 4i) as well as a randomly selected potential line profiling (Figure 4j) shows synchronous variation to the topography. The sample reveals relatively uniform distribution of surface topography and potential, indicating few surface defects and defect-induced potential fluctuation, which is beneficial for PEC performance improvement.[41] Furthermore, slightly higher potential at grain boundaries (GBs) as compared to that of grain interiors (GIs) can also be observed, such GBs can attract the minority carriers (electrons in p-type absorber layer) and repel the majority carriers (holes), thus reducing electron-hole recombination at GBs, enhancing the collection of minority carriers and providing a current route for the minority carriers to the interface, and therefore higher J_{ph} and HC-STH.

Energy band information of CZTSSe absorber layer and CdS buffer layer were analyzed through ultraviolet photoelectron spectroscopy (UPS), as depicted in **Figure 5**a-b. According to valence band (V_B) position and the secondary electron cut-off (SEC) edge, the conduction band (E_C, vs. vacuum) of CZTSSe is –3.46 eV.[42] Compared with the normal hydrogen electrode (NHE), it is –0.98 V_{NHE}, implementing the conversion by using the equation:[43]

$$Energy\ (vs.vacuum) = -eE_{appl}(vs.NHE) - 4.44\ eV \quad (9)$$

The conduction band bottom (C_{BM}) of CZTSSe is obviously located above the reduction potential of hydrogen (i.e., E_{H^+/H_2} of 0 V_{NHE}), which thermodynamically

favors the water reduction occurrence with hydrogen production via solar water splitting, accounting for an interesting J_{ph} that close to its theoretical value. Mott-Schottky (*M-S*) characterizations were further introduced to detect the capacitance formed at semiconductor-electrolyte interface in relative of the applied potential (*V*, i.e., the aforementioned E_{appl}). Figure 5c shows that the $1/C^2$ decreases with potential *V* under the presence of space charge region (SCR), indicating evident p-type characteristic for CZTSSe film. The flat band potential (E_{fb}) and acceptor density (N_A) were obtained according to the following equations:[44]

$$\frac{1}{C_{sc}^2} = -\frac{2}{eA^2\varepsilon\varepsilon_0 N_A}(E_{appl} - E_{fb} - \frac{k_B T}{e}) \quad (10)$$

where C_{sc} represents the SCR capacitance formed by semiconductor-electrolyte contact, ε is the relative dielectric coefficient, ε_0 is the vacuum permittivity, *e* is the unit charge, *A* is active device area, N_A is the acceptor density, k_B is Boltzmann constant, and *T* illustrates temperature. It reveals that the N_A (5.70×10^{17} cm^{-3}) belonging to CZTSSe-2 thin film is significantly lower than that of CZTSSe-1 (2.51×10^{19} cm^{-3}) and even CZTSSe-3 (6.25×10^{17} cm^{-3}) (Figure 5c and Figure S6), indicating fewer acceptor (e.g., Cu_{Sn} antisites) under optimal thickness and preparation process. The valence band position of CZTSSe can also be calculated from E_{fb}, N_A, effective density of states function in the valance band (N_v), and effective mass of hole (m_p^*), according to the formula below:[45]

$$E_v = E_{fb} + kTln(\frac{N_v}{N_A}) \quad (11)$$

$$N_v = 2(\frac{2\pi m_p^* kT}{h^2})^{\frac{3}{2}} \quad (12)$$

The CZTSSe thin films possess quite similar E_V value (–4.52 eV), and it matches well with the UPS measurement derived E_V of –4.52 eV. Similarly, an obvious n-type conductive character can be observed in CdS thin film, and the E_{fb} is estimated to –0.43 V_{NHE} (Figure 5d). Finally, energy band alignment and band bending for CZTSSe/CdS heterojunction is depicted in Figure 5e. Wherein, the conduction band offset (CBO) is examined by an electron affinity (χ)

model, i.e., the χ discrepancy between CZTSSe and CdS, the determined CBO value of −0.20 eV follows the optimum values for high-quality p-n heterojunction (i.e., between a spike of ca. 0.4 eV and a cliff of ca. 0.2 eV).[46] According to previous report, it is favorable for simultaneously suppressing carrier recombination at interface and enhancing the carrier transfer across the interface.[47] In addition, the split of quasi-Fermi levels including the hole quasi-Fermi level (E_{qFp}) and the electron quasi-Fermi level (E_{qFn}) under illumination are also portrayed in Figure 5e, the ideal photovoltage (V_{ph}) determines the maximum onset potential (V_{on}). Afterwards, to gain a deeper insight of the nature of this CZTSSe/CdS heterojunction interface and its effect on photoelectric device performance, the corresponding photovoltaic devices with similar device configuration (i.e., Mo/CZTSSe/CdS/ITO/Ag) were fabricated, and labeled as PV-1, PV-2 and PV-3, respectively. According to the current density-voltage (*J-V*) and external quantum efficiency (EQE) characterizations (Figure S7), the detailed PV performance are plotted in Figure S8 and Table S3, presenting synchronous variation with the corresponding PEC performance. Notably, the highest efficiency of 12% is comparable to the most advanced CZTSSe photovoltaic devices, indicating high-quality solution processed CZTSSe thin film and CZTSSe/CdS heterojunction demonstrated in this work. Figure 5f shows the device $1/C^2$-*V* curves, from which the built-in voltage (V_{bi}) can be evaluated by linear fitting and extrapolation. By contrast, a slightly higher V_{bi} value (0.53 V) belonging to PV-2 confirms an improved CZTSSe-2/CdS heterojunction quality, which can facilitate the separation of photo-generated carriers. In general, Capacitance-voltage (*C-V*) measures the capacitance responses including interface defects, bulk defects and free carriers, whereas Drive-level capacitance profiling (*DLCP*) measurement corresponds to the responses of bulk defects and free carriers.[48] Thus, the interface defect density (N_i) can be

obtained by the difference between *C-V* and *DLCP* at 0 V voltage (Figure 5g). The derived N_i values are listed in Table S4, obviously, the N_i of 1.30×10^{15} cm^{-3} for device PV-2 is smaller than that of the other two devices, strengthening the suppressed interface defects and defects-assisted recombination. Moreover, PV-2 device possesses a larger depletion width (W of 213 nm) compared with PV-1 (W of 135 nm) and PV-3 (W of 156 nm) devices, echoing the prediction that W varies positively with V_{bi},[49] which can also accelerate the charge carrier separation and extraction. The Urbach energy (E_u) is an important indicator with respect to band tailing effect, which is availably determined by plotting ln(−ln(1−EQE)) versus energy (Figure 5h).[50] A minimum E_u value of 26.7 meV for device PV-2 confirms that nonradiative recombination near the heterojunction region is positively mitigated.

Finally, to monitor the defect distribution inside the bulk absorber layer, temperature-dependent admittance spectra were recorded. **Figure 6**a-c displays the capacitance spectra of device PV-1, PV-2 and PV-3 measured at various temperatures (i.e., T decreasing from 300 K to 110 K) and frequency (i.e., f increasing from 10^3 to 10^6 Hz). The transition frequency at each step is connected with the rate of carrier trapping and emission from intrinsic bulk defect states in CZTSSe thin film.[51] Obviously, they will shift to higher frequency with the increase of temperature. Thus, for p-type CZTSSe semiconductor, the occupation of hole traps in SCR possesses an energy gap of $E_a = E_T - E_V$ above the valence, where E_a represents activation energy, E_T is trap energy, E_V is valence energy. Arrhenius plots of the transition frequencies are plotted in Figure 6d-f, wherein, E_a values can be extracted through fitting. The differential capacitance spectrum at each temperature is superimposed to produce an energy defect distribution ($N_T(E_\omega)$) according to the following equations:[52]

$$E(\omega) = kT \ln(\frac{2\pi v_0 T^2}{\omega}) \quad (13)$$

$$N_T(E_\omega) = -\frac{V_{bi}}{qWkT}\frac{\omega dC}{d\omega} \quad (14)$$

where v_0 is the emission factor, ω is the applied frequency. V_{bi} and W are obtained from the *C-V* measurements, as aforementioned in Figure 5. Based on the theoretical basis of first principle and experimental results reported in the literature, the Cu_{Zn} antisite defect has comparatively lower formation energy than the copper vacancy (V_{Cu}).[53] The defect of acceptor with E_a in the range of 0.13–0.2 eV can be attributed to Cu_{Zn} antisite defect, and a shallower acceptor level at ~0.05 eV above the valence band maximum (V_{BM}) is considered to V_{Cu}. Thus, defect energy distribution in device PV-2 with peak value located at 0.0785 eV can be ascribed to V_{Cu}. However, in the device PV-1 and PV-3, the values shift to 0.135 eV and 0.199 eV, respectively, which can be assigned to Cu_{Zn} antisite. It has been proved that V_{Cu} with shallow acceptor level is much preferable than Cu_{Zn} antisite for achieving high-performance photoelectric devices.[53] Moreover, as a Gaussian distribution for defect states fitting, the integrated defect density N_T of device PV-2 is 6.51×10^{14} cm^{-3} belonging to V_{Cu}, which is really benign as compared to that Cu_{Zn} antisite with N_T values of 4.34×10^{16} cm^{-3} and 9.16×10^{14} cm^{-3} in PV-1 and PV-3 devices, respectively (Figure 6h-i). Overall, CZTSSe-2 with suitable thickness can modify the bulk defect characters under thermodynamic/kinetic growth process, which is beneficial to suppress detrimental defects, and therefore to improve device performance.

3. Conclusions

In conclusion, CZTSSe light absorbing thin films with high crystallinity and large compact crystals can be fulfilled via 2-ME solvents assisted spin coating of precursor, and selenization induced thermodynamic/kinetic crystal growth. Mo/CZTSSe/CdS/TiO_2/Pt planar-type photocathodes were fabricated, and the device

performance were systematically investigated. The CZTSSe absorber layer quality has been found to obviously influence the PEC performance. Under an optimal thickness of ~1.6 μm, it exhibited much benign bulk defects with shallower acceptor level and reduced defect density, much superior CZTSSe/CdS heterojunction with larger built-in voltage and less interface defect density. Thanks to the suppressed defects-assisted recombination, as well as significantly enhanced charge transfer efficiency of 99.20% and charge separation efficiency of 95.04%, highly interesting J_{ph} of 40.40 mA/cm^2 (at 0 V_{RHE}) can be achieved, which is quite close to its theoretical J_{ph} value of 42.85 mA/cm^2, representing the record value for kesterites-based photocathodes reported to date. Furthermore, the champion CZTSSe photocathode with intriguing HC-STH conversion efficiency of 6.47% is also comparable to those state-of-the-art chalcogenide-based photocathodes. This work can lead to a deeper exploration of narrow band-gap photoelectrode materials, and the further development of solar hydrogen production via PEC water splitting.

4. Experimental Section

Preparation of CZTSSe thin film: The CZTS precursor solutions were prepared using some available materials, to be specific, the Sn^{4+} and Sn^{2+} precursor solutions were separately prepared by dissolving $SnCl_4 \cdot 5H_2O$ (0.83 M), CuCl (1.42 M), $Zn(CH_3COO)_2 \cdot 2H_2O$ (1.0 M), $SC(NH_2)_2$ (6.4 M), and $SnCl_2 \cdot 2H_2O$ (0.83 M), $Cu(CH_3COO)_2 \cdot H_2O$ (1.42 M), $ZnCl_2$ (1.0 M) and $SC(NH_2)_2$ (6.4 M) into 2-ME organic solvents. After mixing them at 60 °C for 90 min, a yellow CZTS precursor solution was obtained, and then diluted to half of its pristine concentration. The CZTS precursor films were prepared via spin coating method using molybdenum (Mo)-coated soda-lime glass (SLG) as substrates, which were repeated for specific times (i.e., 8, 10 and 12 times in this work) under 3000 rpm for 30 s, and then underwent heat treatment at 280 °C for 90 s on a hot-plate in ambient condition. Afterwards, CZTSSe thin

film was obtained by annealing the CZTS precursor film in selenium atmosphere, wherein, the thin film and selenium particles were put into a sealed graphite box, running a two-step rapid thermal process including a first heat treatment to 80 °C with ramping rate of 4 °C/s, and then rapidly heated to 550 °C with ramping rate of 5 °C/s. After 20 min dwelling, the sample was cooled down naturally in furnace.

Preparation of CZTSSe photocathode: Following the preparation of CZTSSe light absorbing layer, buffer layer of CdS was coated by chemical bath deposition (CBD) process. The deionized water (140 ml), thiourea (0.75 M, 20 ml), $CdSO_4$ (0.015 M, 20 ml), and ammonia solution (14.8 M, 22 ml) were poured successively into a specific container containing SLG/Mo/CZTSSe pieces. Then, it was placed into a water bath with slowly stirring at 80 °C for 10 mins. The samples were dried in an oven after being rinsed with deionized water. The TiO_2 protective layer was deposited using a NaFeng NCR-200R Atomic Layer Deposition (ALD) system, using H_2O and $TiCl_4$ as the O and Ti precursors, respectively. Thickness of TiO_2 was kept at 10 nm under a growth rate of 0.7 Å per cycle. Pt co-catalyst was then introduced through a 108 Auto Sputter Coater under a DC current of 20 mA and a duration of 50 s. Accordingly, SLG/Mo/CZTSSe/CdS/TiO_2/Pt thin-film photocathode was fabricated. Before measuring device performance, Ag colloids were painted onto the as-exposed Mo substrate surface to form metal contact.

Characterizations: Crystallinity and structure of CZTSSe thin films were examined with CuK_α radiation in X-ray diffractometer (XRD, Ultima-iv). Surface and cross-sectional morphologies were observed by scanning electron microscope (SEM, Zeiss SUPRA 55). Topographies and surface potentials of CZTSSe were also examined via a Kelvin probe force microscope (KPFM, Bruker Dimension ICON). Microstructure of the CZTSSe-based photocathode was further characterized using a transmission electron microscope (TEM, FEI Titan Cubed Themis G2 300). Reflection spectra and absorption spectra of CZTSSe were acquired from Shimadzu

UV-3600 spectrophotometer. Ultraviolet photoelectron spectroscopy (UPS) was evaluated by PHI 5000 VersaProbe with He I source of 21.22 eV. The PEC performance was measured using a CHI 660E electrochemical workstation under typical three-electrode model, wherein, Pt-foil was used as the counter electrode, Ag/AgCl in saturated KCl solution as the reference electrode, and the CZTSSe photocathode as working electrode. Photoelectrochemical impedance spectroscopy (PEIS) was evaluated under simulated sunlight illumination with frequencies range from 10 Hz to 10^5 Hz. Mott-Schottky (*M-S*) measurements were implemented to extract the flat band potential (E_{fb}) of the CZTSSe and CdS film samples. Capacitance-voltage (*C-V*) tests were carried out at 30 mV AC amplitude and 10^4 Hz frequency, and scanning voltage from −0.50 V to 0.10 V under dark condition. Drive-level capacitance profiling (*DLCP*) analysis were performed with AC amplitude from 20 mV to 140 mV, accompanied with DC voltage from −0.25 V to 0 V. The device admittance spectroscopy (AS) was obtained in a Janis VPF-100 cryostat, covering frequency range from 10^2 Hz to 10^6 Hz and temperature range from 300 K to 110 K (Lake Shore, 325 Cryogenic Temperature Controller).

Supporting Information

Supporting Information is available from the Wiley Online Library or from the author.

Acknowledgements

This work was supported by National Natural Science Foundation of China (No. 62074102, 62104156), Guangdong Basic and Applied Basic Research Foundation (2022A1515010979, 2023A1515011256) China, Science and Technology plan project of Shenzhen (20220808165025003, 20200812000347001) China. The authors wish to acknowledge the assistance on (TEM/STEM/FIB) received from the Electron Microscope Center of the Shenzhen University.

Conflict of Interest

The authors declare no conflict of interest.

References

[1] W. Yang, J. Moon, *ChemSusChem* **2019**, 12, 1889-1899.

[2] J. Tan, W. Yang, Y. Oh, H. Lee, J. Park, R. Boppella, J. Kim and J. Moon, *Adv. Energy Mater*. **2019**, 9, 1900179.

[3] C. Ros, T. Andreu, S. Giraldo, V. Izquierdo-Roca, E. Saucedo, J. R. Morante, *ACS Appl. Mater. Interfaces* **2018**, 10, 13425-13433.

[4] Y. Gong, R. Qiu, C. Niu, J. Fu, E. Jedlicka, R. Giridharagopal, Q. Zhu, Y. Zhou, W. Yan, S. Yu, J. Jiang, S. Wu, D. S. Ginger, W. Huang and H. Xin, *Adv. Funct. Mater.* **2021**, 31, 2101927.

[5] S. Chen, T. Liu, M. Chen, M. Ishaq, R. Tang, Z. Zheng, Z. Su, X. Li, X. Qiao, P. Fan and G. Liang, *Nano Energy* **2022**, 99, 107417.

[6] C. Li, T. Hisatomi, O. Watanabe, M. Nakabayashi, N. Shibata, K. Domen, J. J. Delaunay, *Appl. Phys. Lett*. **2016**, 109, 033902.

[7] C. M. Jiang, S. E. Reyes-Lillo, Y. Liang, Y. S. Liu, G. Liu, F. M. Toma, D. Prendergast, I. D. Sharp, J. K. Cooper, *Chem. Mater.* **2019**, 31, 2524.

[8] A. D. DeAngelis, K. Horsley, N. Gaillard, *J. Phys. Chem. C* **2018**, 122, 14304-14312.

[9] M. Li, R. Zhao, Y. Su, J. Hu, Z. Yang, Y. Zhang, *Appl. Catal. B Environ.* **2017**, 203, 715-724.

[10] J. Zhao, T. Minegishi, H. Kaneko, G. Ma, M. Zhong, M. Nakabayashi, T. Hisatomi, M. Katayama, N. Shibata, T. Yamada, K. Domen, *Chem. Commun.,* **2019**, 55, 470-473.

[11] M. Chen, Y. Liu, C. Li, A. Li, X. Chang, W. Liu, Y. Sun, T. Wang, J. Gong, *Energy Environ. Sci.* **2018**, 11, 2025-2034.

[12] B. Koo, D. Kim, P. Boonmongkolras, S. R. Pae, S. Byun, J. Kim, J. H. Lee, D. H. Kim, S. Kim, B. T. Ahn, S. W. Nam, B. Shin, *ACS Appl. Energy Mater.* **2020**, 3, 2296-2303.

[13] N. Guijarro, M. S. Prévot, X. Yu, X. A. Jeanbourquin, P. Bornoz, W. Bourée, M. Johnson, F. Le Formal, K. Sivula, *Adv. Energy Mater.* **2016**, 6, 1501949.

[14] J. Song, B. Teymur, Y. Zhou, E. Ngaboyamahina, D. B. Mitzi, *ACS Appl. Energy Mater.* **2021**, 4, 81-87.

[15] D. Huang, K. Wang, L. Li, K. Feng, N. An, S. Ikeda, Y. Kuang, Y. Ng, F. Jiang, *Energy Environ. Sci.* **2021**, 14, 1480-1489.

[16] J. Tan, B. Kang, K. Kim, D. Kang, H. Lee, S. Ma, G. Jang, H. Lee, J. Moon, *Nat. Energy*

2022, 7, 537-547.

[17] J. Tan, W. Yang, H. Lee, J. Park, K. Kim, O. S. Hutter, L. J. Phillips, S. Shim, J. Yun, Y. Park, J. Lee, J. D. Major, J. Moon, *Appl. Catal. B Environ.* **2021**, 286, 119890.

[18] I. Repins, M. A. Contreras, B. Egaas, C. DeHart, J. Scharf, C. L. Perkins, B. To, R. Noufi, *Prog. Photovolt: Res. Appl.* **2008**, 16, 235-239.

[19] G. X. Liang, Z. X. Yu, Z. G. Xie, Y. He, J. H. Lin, S. Chen, Z. H. Zheng, J. T. Luo, P. Fan, Z. H. Su, H. L. Ma, X. H. Zhang, *Sol. RRL* **2021**, 5, 2100574.

[20] T. Todorov, H. W. Hillhouse, S. Aazou, Z. Sekkat, O. Vigil-Galán, S. D. Deshmukh, R. Agrawal, S. Bourdais, M. Valdés, P. Arnou, D. B. Mitzi, P. J. Dale, *J. Phys. Energy* **2020**, 2, 012003.

[21] W. Wang, M. T. Winkler, O. Gunawan, T. Gokmen, T. K. Todorov, Y. Zhu, D. B. Mitzi, *Adv. Energy Mater.* **2014**, 4, 1301465.

[22] Y. Gong, Y. Zhang, E. Jedlicka, R. Giridharagopal, J. A. Clark, W. Yan, C. Niu, R. Qiu, J. Jiang, S. Yu, S. Wu, H. W. Hillhouse, D. S. Ginger, W. Huang, H. Xin, *Sci. China Mater.* **2021**, 64, 52-60.

[23] H. Q. Xiao, W. H. Zhou, D. X. Kou, Z. J. Zhou, Y. N. Meng, Y. F. Qi, S. J. Yuan, Q. W. Tian, S. X. Wu, *Green Chem.* **2020**, 22, 3597-3607.

[24] Y. Cui, M. Wang, P. Dong, S. Zhang, J. Fu, L. Fan, C. Zhao, S. Wu, Z. Zheng, *Adv. Sci.* **2022**, 9, 2201241.

[25] Y. Zhao, Z. Yu, J. Hu, Z. Zheng, H. Ma, K. Sun, X. Hao, G. Liang, P. Fan, X. Zhang, Z. Su, *J. Energy Chem.* **2022**, 75, 321.

[26] X. Y. Chen, M. Ishaq, N. Ahmad, R. Tang, Z. H. Zheng, J. G. Hu, Z. H. Su, P. Fan, G. X. Liang, S. Chen, *J. Mater. Chem. A* **2022**, 10, 22791-22802.

[27] W. Yang, J. H. Kim, O. S. Hutter, L. J. Phillips, J. Tan, J. Park, H. Lee, J. D. Major, J. S. Lee, J. Moon, *Nat. Commun.* **2020**, 11, 861.

[28] M. Cao, X. Zhang, H. Gong, Y. Sun, S. Zhang, Y. Jiang, J. Zhang, Y. Shen, L. Wang, *Ceram. Int.* **2021**, 47, 25921.

[29] Y. Zhou, D. Shin, E. Ngaboyamahina, Q. Han, C. B. Parker, D. B. Mitzi, J. T. Glass, *ACS Energy Lett.* **2018**, 3, 177.

[30] S. Grau, S. Giraldo, E. Saucedo, J. R. Morante, A. Llobet, C. Gimbert-Suriñach, *J. Mater. Chem. A* **2019**, 7, 24320.

[31] X. Wu, W. Zhao, Y. Hu, G. Xiao, H. Ni, S. Ikeda, Y. Ng, F. Jiang, *Adv. Sci.* **2022**, 9, 2204029.

[32] J. Su, T. Minegishi, K. Domen, *J. Mater. Chem. A* **2017**, 5, 13154.

[33] Y. Gong, Y. Zhang, Q. Zhu, Y. Zhou, R. Qiu, C. Niu, W. Yan, W. Huang, H. Xin, *Energy Environ. Sci.* **2021**, 14, 2369-2380.

[34] Y. Li, H. X. Zhang, Y. Zhao, X. F. Dong, T. T. Zheng, C. W. Wang, *Appl. Surf. Sci.* **2020**, 516, 145872.

[35] H. Guo, G. Wang, R. Meng, Y. Sun, S. Wang, S. Zhang, J. Wu, L. Wu, G. Liang, H. Li, Y. Zhang, *J. Mater. Chem. A* **2020**, 8, 22065-22074.

[36] G. P. Joshi, N. S. Saxena, R. Mangal, A. Mishra, T. P. Sharma, *Mater. Sci. Bull.* **2003**, 26, 387-389.

[37] T. Zhou, S. Chen, J. Wang, Y. Zhang, J. Li, J. Bai, B. Zhou, *Chem. Eng. J.* **2021**, 403, 126350.

[38] D. Klotz, D. A. Grave, A. Rothschild, *Phys. Chem. Chem. Phys.* **2017**, 19, 20383-20392.

[39] G. Liang, T. Liu, M. Ishaq, Z. Chen, R. Tang, Z. Zheng, Z. Su, P. Fan, X. Zhang, S. Chen, *Chem. Eng. J.* **2022**, 431, 133359.

[40] P. Fan, Y. He, G. Liang, Z. Xie, Z. Yu, J. Lin, S. Chen, Z. Zheng, J. Luo, Z. Su, *J. Mater. Chem. A* **2021**, 9, 25196-25207.

[41] Y. H. Jo, J.W. Jang, B. C. Mohanty, H. B. Kang, Y. S. Cho, *J. Phys. D: Appl. Phys.* **2015**, 48, 245103.

[42] S. Chen, X. Liu, X. Qiao, X. Wan, K. Shehzad, X. Zhang, Y. Xu, X. Fan, *Small* **2017**, 13, 1604033.

[43] R. Beranek, *Adv. Phys. Chem.* **2011**, 2011, 786759.

[44] K. Gelderman, L. Lee, S.W. Donne, *J. Chem. Educ.* **2007**, 84, 685.

[45] S. Trasatti, **1986**, 58, 955.

[46] L. Zhang, Y. Li, C. Li, Q. Chen, Z. Zhen, X. Jiang, M. Zhong, F. Zhang, H. Zhu, *ACS Nano* **2017**, 11, 12753-12763.

[47] S. Chen, Y. Fu, M. Ishaq, C. Li, D. Ren, Z. Su, X. Qiao, P. Fan, G. Liang, J. Tang, *InfoMat* **2023**, https://doi.org/10.1002/inf2.12400.

[48] Z. Su, G. Liang, P. Fan, J. Luo, Z. Zheng, Z. Xie, W. Wang, S. Chen, J. Hu, Y. Wei, C. Yan, J. Huang, X. Hao, F. Liu, *Adv. Mater.* **2020**, 32, 2000121.

[49] G. Liang, M. Chen, M. Ishaq, X. Li, R. Tang, Z. Zheng, Z. Su, P. Fan, X. Zhang, S. Chen, *Adv. Sci.* **2022**, 9, 2105142.

[50] R. Tang, S. Chen, Z. H. Zheng, Z. H. Su, J. T. Luo, P. Fan, X. H. Zhang, J. Tang, G. X. Liang, *Adv. Mater.* **2022**, 34, 2109078.

[51] H. S. Duan, H. Zhou, Q. Chen, P. Sun, S. Luo, T. B. Song, B. Bob, Y. Yang, *Phys. Chem. Chem. Phys.* **2015**, 17, 112-116.

[52] R. Herberholz, M. Igalson, H. W. Schock, *J. Appl. Phys.* **1998**, 83, 318-325.

[53] S. Chen, A. Walsh, X. G. Gong, S. H. Wei, *Adv. Mater.* **2013**, 25, 1522-1539.

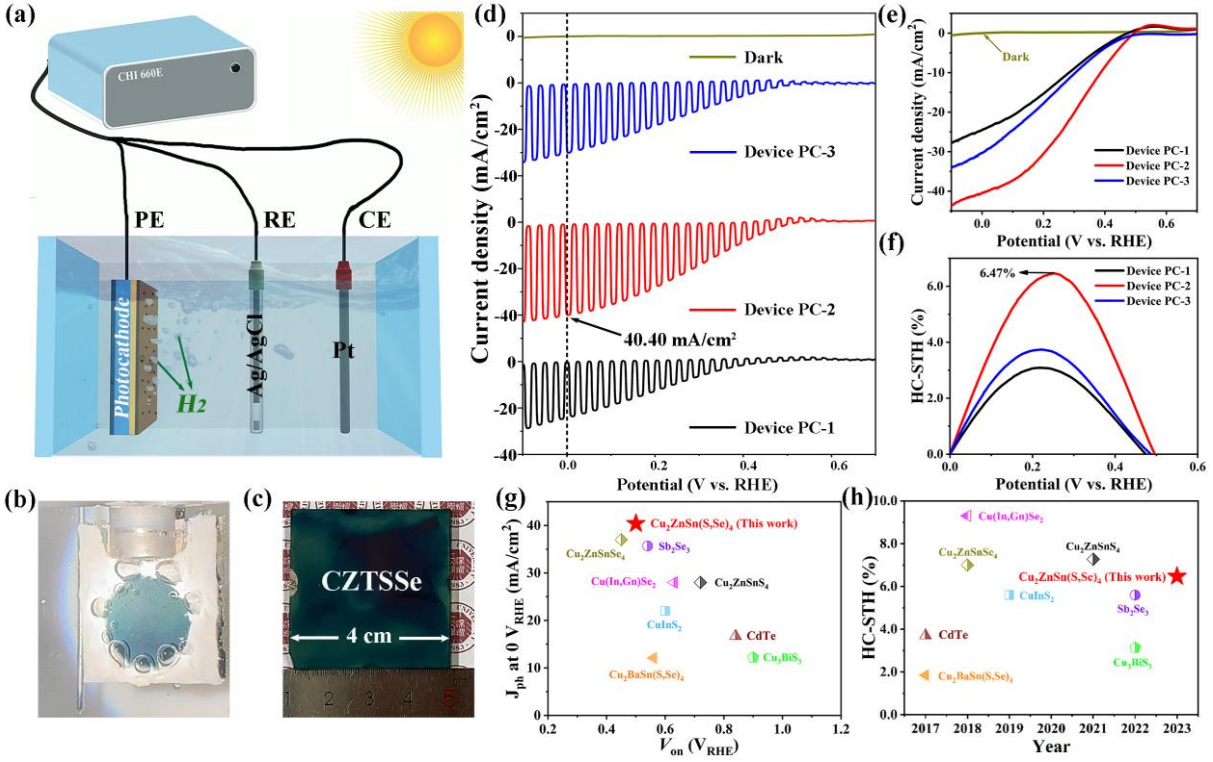

Figure 1. (a) Schematic diagram of a 3-electrode PEC measurement. (b) A photo of hydrogen bubbles produce from photocathode surface and move to the electrolyte. (c) Photograph of a representative 4×4 cm^2 CZTSSe photocathode. (d) *J*-*V* curves of the photocathodes under dark and chopped sunlight illumination. (e) *J*-*V* curves of the photocathodes under dark and continuous sunlight illumination. (f) The calculated HC-STH conversion efficiencies. (g-h) A comparison of this work to those of state-of-the-art chalcogenide-based photocathodes.

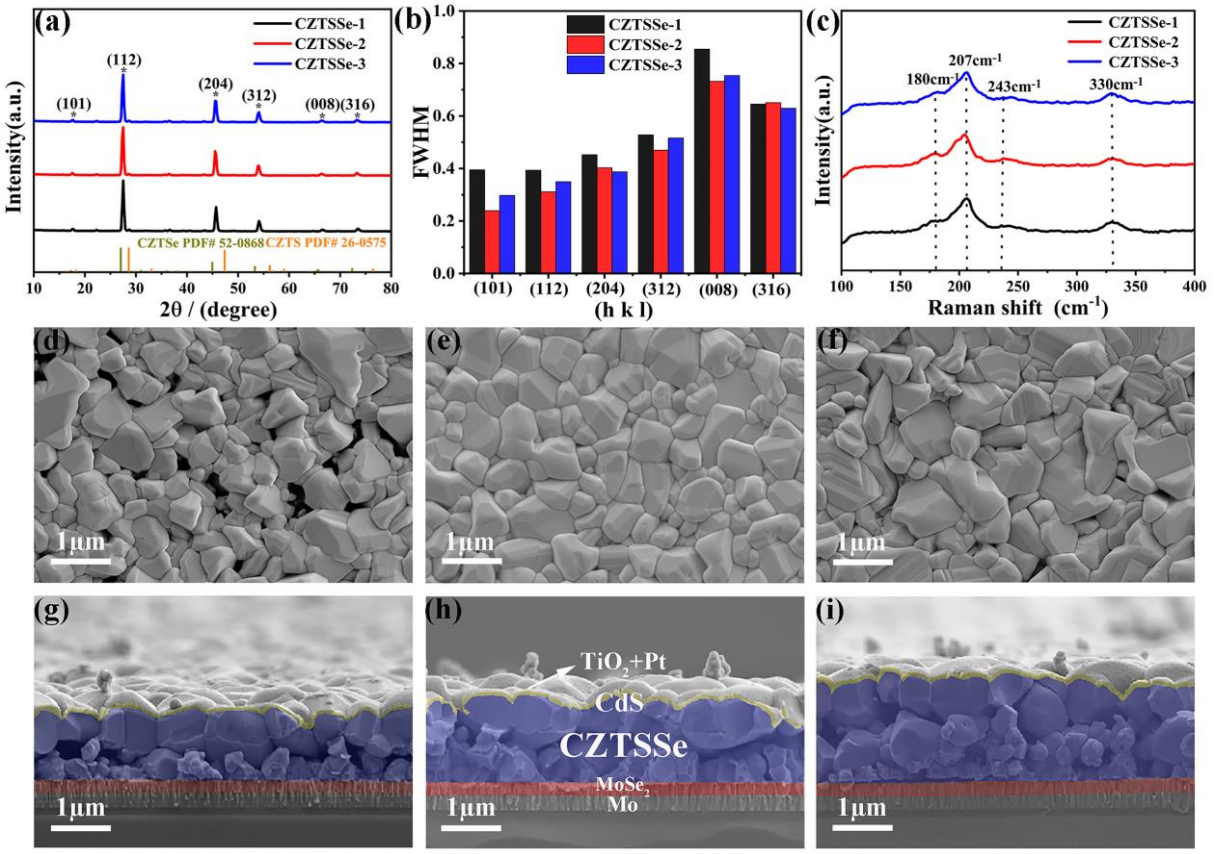

Figure 2. (a) XRD patterns, (b) FWHM of the diffraction peaks, and (c) Raman spectra of the CZTSSe thin films with different thicknesses. (d-f) Top-view SEM images of the CZTSSe thin films. (g-i) Cross-sectional SEM images of the CZTSSe-based photocathodes.

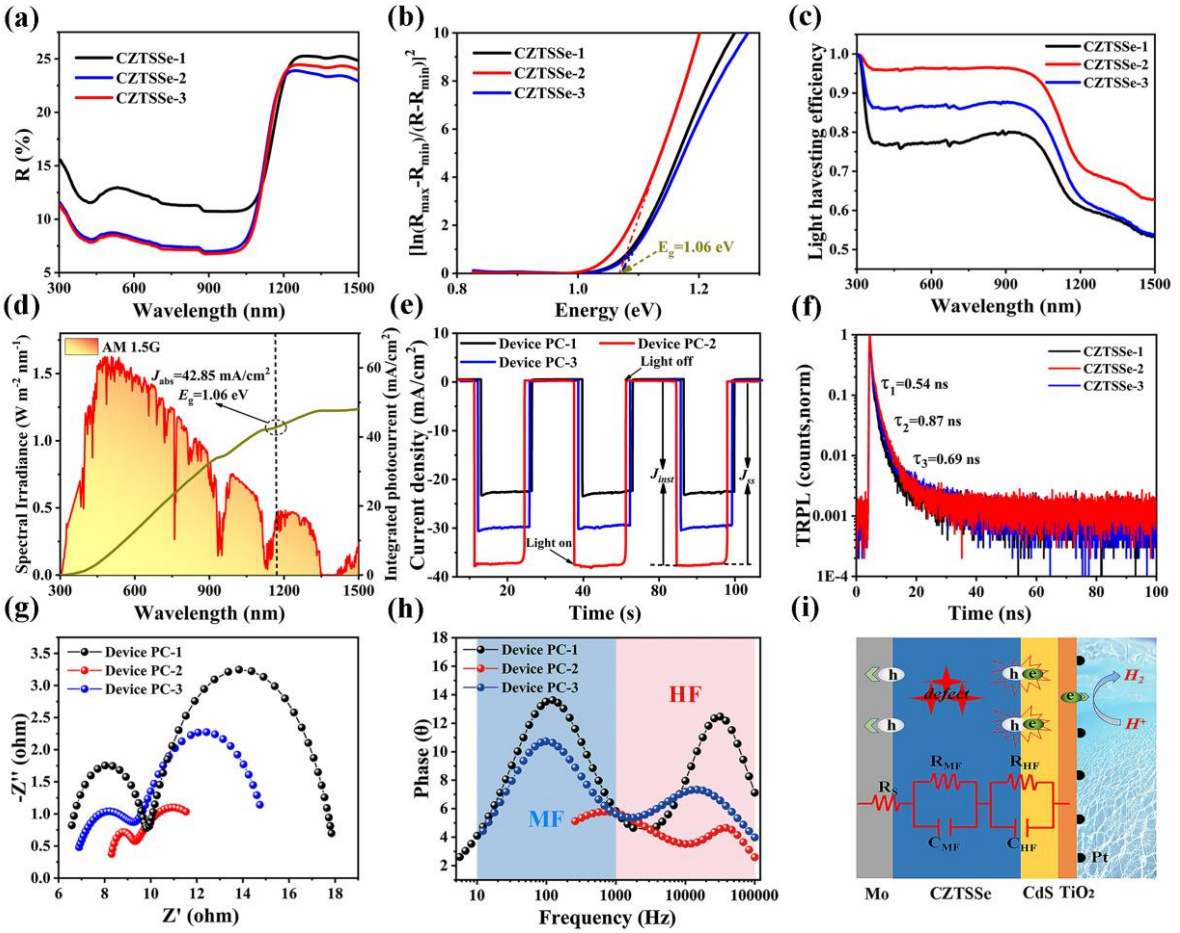

Figure 3. (a) Reflection spectra, (b) Plots of $[\ln (R_{max}- R_{min})/(R- R_{min})]^2$ versus Energy, and (c) Light harvesting efficiency (LHE) of CZTSSe thin films with different thicknesses. (d) The energy density flux for the standard AM 1.5G solar spectrum, along with the integrated photocurrent density of the CZTSSe-2. (e) Transient photocurrent response of devices PC-1, PC-2 and PC-3. (f) Time-resolved photoluminescence characters for CZTSSe thin films. (g) Nyquist plots, and (h) the corresponding Bode plots of the CZTSSe-based photocathodes. (i) Schematic diagram and equivalent circuit system associated with the charge transfer processes.

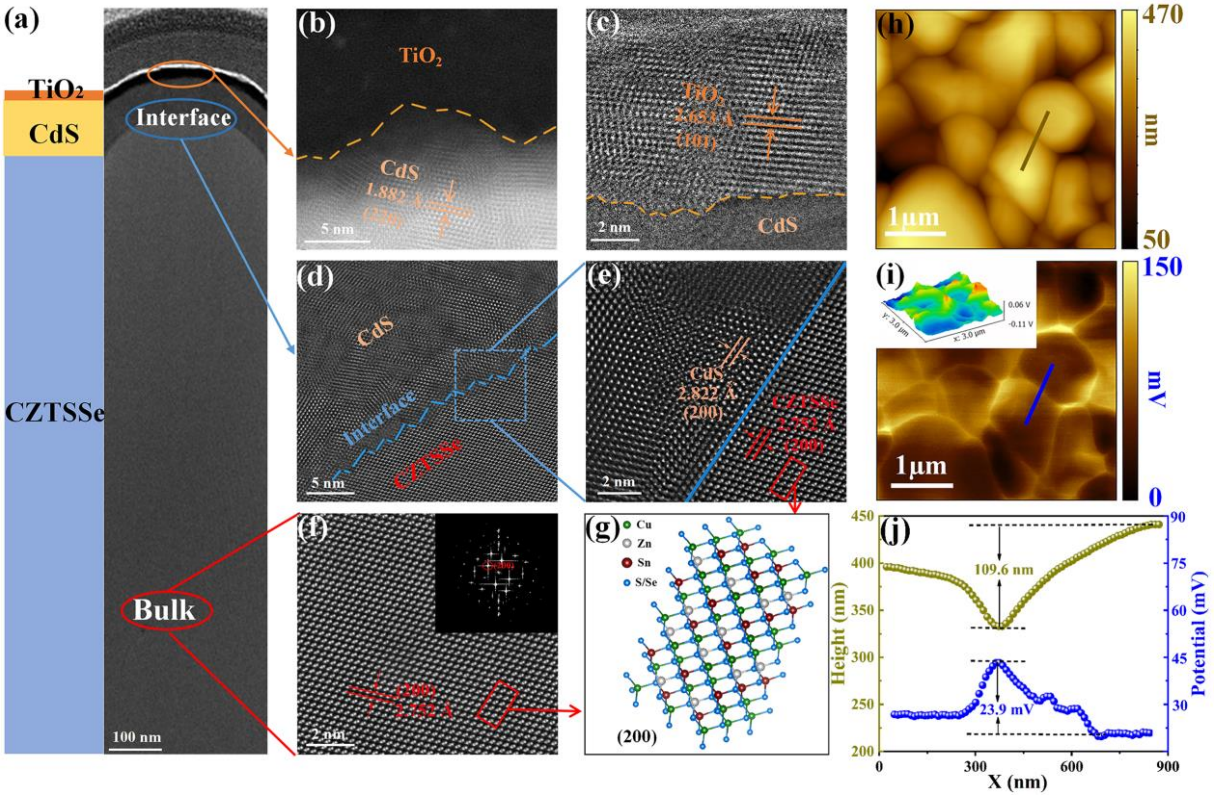

Figure 4. TEM characterizations of a Mo/CZTSSe/CdS/TiO_2/Pt photocathode. (a) Cross-sectional TEM image. (b, c) HRTEM images of CdS/TiO_2 interface. (d, e) HRTEM images of CZTSSe/CdS heterojunction interface. (f) HRTEM image of CZTSSe bulk absorber layer, accompanied with a SAED pattern (inset), and (g) the corresponding atomic configuration of (200) crystal plane of CZTSSe. (h) Topography and (i) Surface potential of CZTSSe-2 thin film acquired from KPFM analysis, a potential mapping is also inserted in (i). (j) Topography and potential line profiles derived from scanning the yellow and blue lines in (h) and (i), respectively.

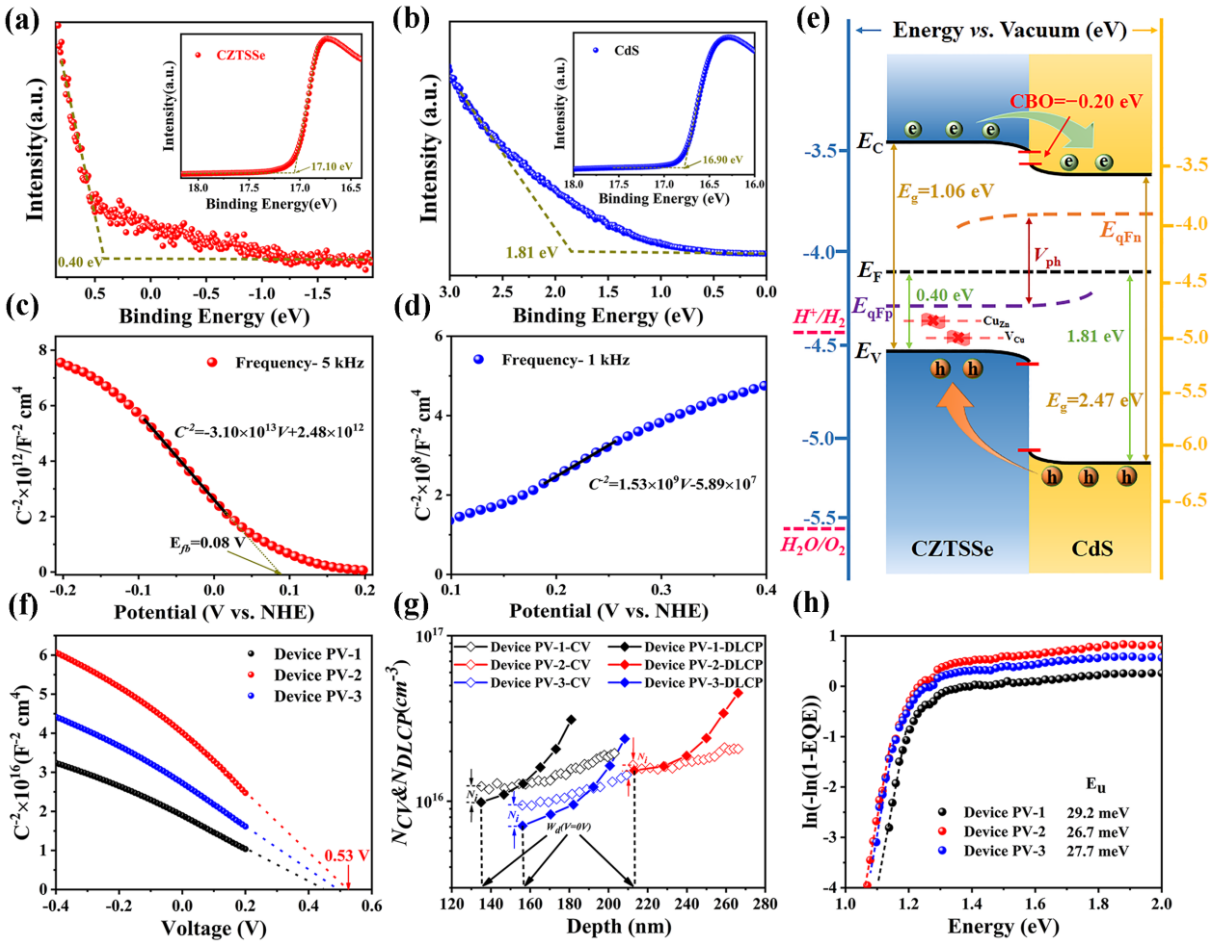

Figure 5. (a) UPS characterizations derived V_B position and SEC edge of CZTSSe thin film. (b) The corresponding plots for CdS thin film. *M-S* plots of CZTSSe at frequency of 5 kHz (c), and CdS at frequency of 1 kHz (d). (e) Schematic illustration of energy band alignment, band bending, and the split of quasi-fermi levels of the CZTSSe/CdS heterojunction, along with representative defect energy levels. (f) $1/C^2$-*V* plots, (g) *C-V* and *DLCP* profiles, and (h) ln (ln (1–EQE)) versus energy plots of the CZTSSe-based photovoltaic devices.

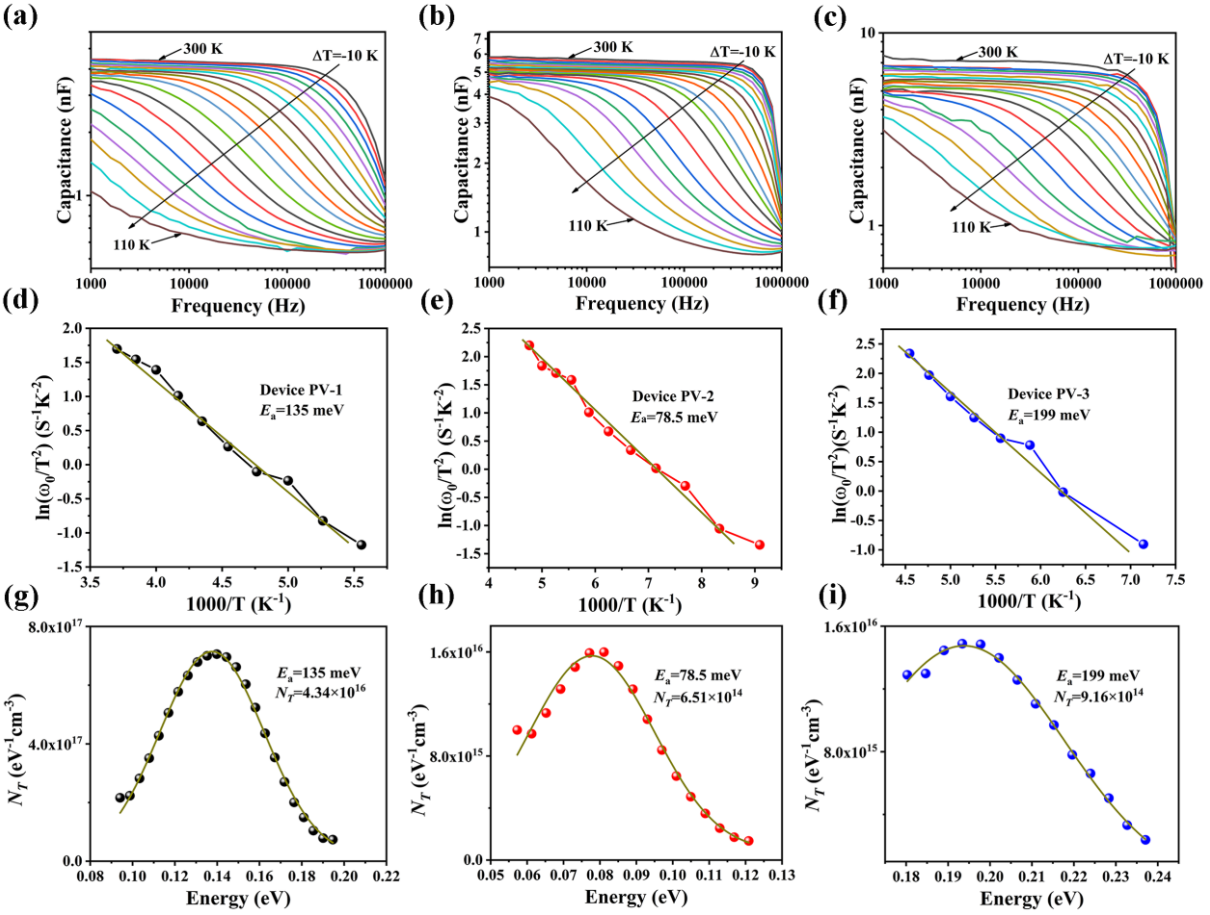

Figure 6. Temperature-dependent admittance characterizations of the CZTSSe-based photovoltaic devices. (a-c) Capacitance variation at different frequency and temperature. (d-f) Arrhenius plots of the characteristic frequencies to obtain the defect activation energy. (g-i) The corresponding defect distributions.

Table of contents: Two-step process involving solution processed spin coating and selenization processed thermodynamic/kinetic growth of high-quality CZTSSe thin film is presented. Under an appropriate film thickness, it can significantly suppress carrier recombination and enhance charge separation efficiency. Consequently, the champion Mo/CZTSSe/CdS/TiO_2/Pt photocathode delivers a record photocurrent density of 40.4 mA/cm^2, and a stimulating half-cell solar-to-hydrogen conversion efficiency of 6.47%.

*Guangxing Liang, Zhidong Li, Muhammad Ishaq, Zhuanghao Zheng, Zhenghua Su, Hongli Ma, Xianghua Zhang, Ping Fan, and Shuo Chen**

Title: Charge Separation Enhancement Enables Record Photocurrent Density in $Cu_2ZnSn(S,Se)_4$ Photocathodes for Efficient Solar Hydrogen Production

ToC figure

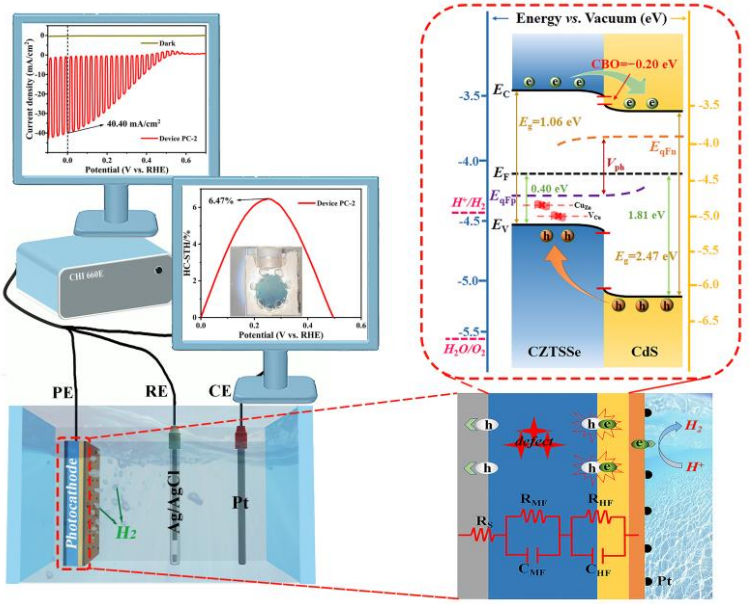

Supporting Information

Charge Separation Enhancement Enables Record Photocurrent Density in $Cu_2ZnSn(S,Se)_4$ Photocathodes for Efficient Solar Hydrogen Production

*Guangxing Liang, Zhidong Li, Muhammad Ishaq, Zhuanghao Zheng, Zhenghua Su, Hongli Ma, Xianghua Zhang, Ping Fan, and Shuo Chen**

Table S1. A comparison of this work to those of previously reported chalcogenide-based photocathodes.

Photocathode	Electrolyte	J_{ph} (mA cm^{-2} at 0 V_{RHE})	V_{on} (V_{RHE})	HC-STH (%)	Year	Ref.
Mo/$Cu_2ZnSn(S,Se)_4$/CdS/TiO_2/Pt	**0.5M H_2SO_4**	**−40.40**	**0.50**	**6.47%**	**2023**	This work
FTO/$Cu_2ZnSn(S,Se)_4$/CdS/TiO_2/Pt	0.5M Na_2SO_4/H_2SO_4	−7.2	/	/	2021	[1]
Mo/$Cu_2BaSn(S,Se)_4$/CdS/TiO_2/Pt	0.5M KH_2PO_4/Na_2SO_4	−5.54	0.39	0.49%	2021	[2]
Mo/$Cu_2BaSn(S,Se)_4$/CdS/TiO_2/Pt	0.5M KH_2PO_4/Na_2SO_4	−12.1	0.56	1.85%	2017	[3]
Mo/Cu_2ZnSnS_4/HfO_2/CdS/HfO_2/Pt	0.2M NaH_2PO_4/Na_2HPO_4	−28	0.72	7.27%	2021	[4]
Mo/$Cu_2ZnSnSe_4$/CdS/ZnO/ITO/MoS_2	Phosphate buffer solution	−18	0.43	/	2019	[5]
Mo/$Cu_2ZnSnSe_4$/CdS/TCO/TiO_2/Pt	0.5M H_2SO_4	−37	0.45	7.0%	2018	[6]
Mo/Cu(In,Ga)Se_2/CdS/Al_2O_3/TiO_2/Pt	1M $HClO_4$	−28	0.63	9.3%	2018	[7]
Mo/$(CuInS_2)_{0.81}(ZnS)_{0.19}$/CdS/Pt	0.5M KPi	−16.7	0.84	5.6%	2019	[8]
Mo/Cu_3BiS_3/$In_{0.6}Cd_{0.4}S$/TiO_2/Pt	0.2M NaH_2PO_4/Na_2HPO_4	−12.2	0.90	3.13%	2022	[9]
Mo/Sb_2Se_3/CdS(In)/TiO_2/Pt	0.5M H_2SO_4	−35.7	0.54	5.6%	2022	[10]
FTO/Au/Cu/CdTe/CdS/Pt	1M KH_2PO_4	−22	0.6	3.7%	2017	[11]

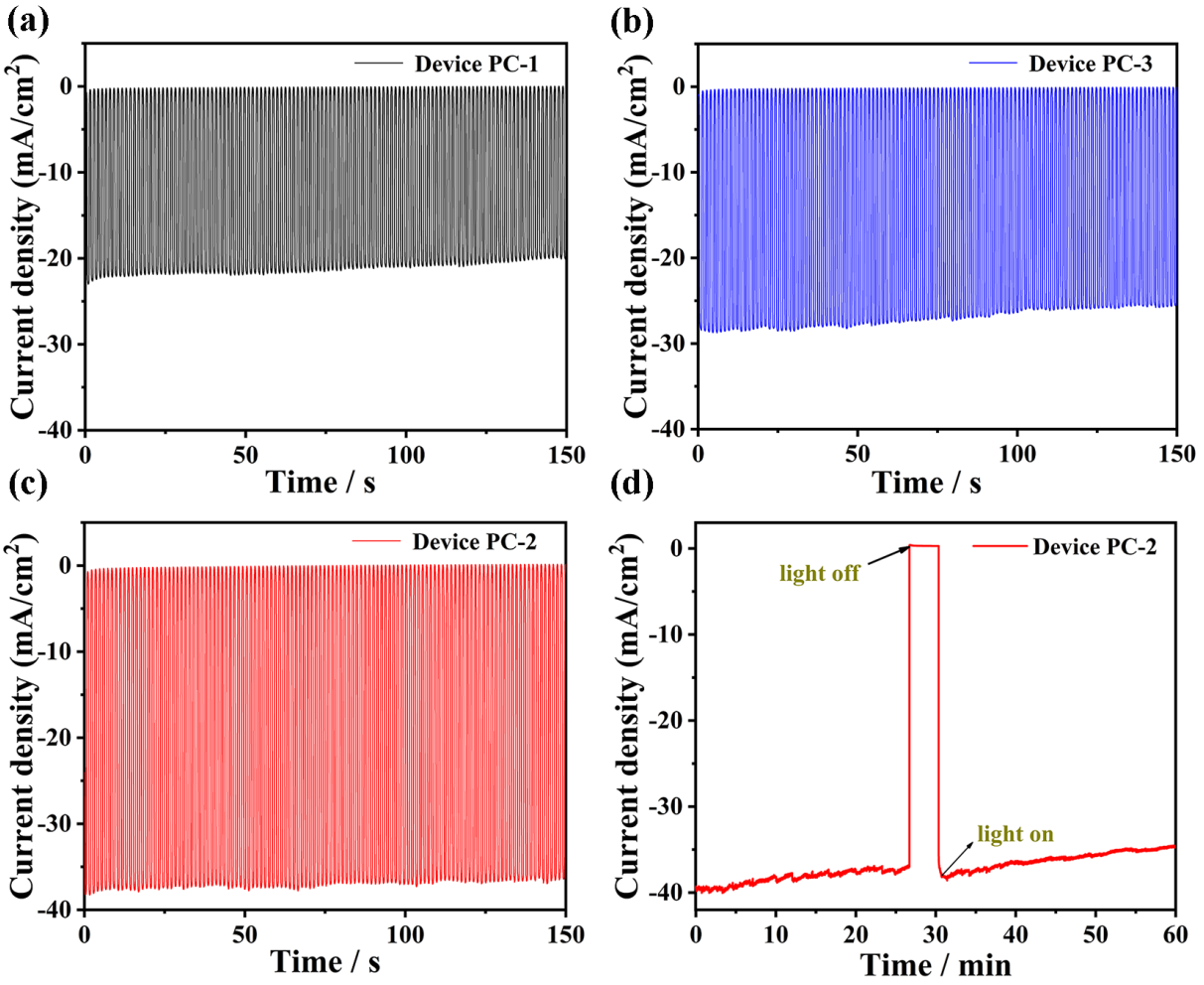

Figure S1. (a-c) Chopped *J-T* curves of the photocathodes at 0 V_{RHE} under AM 1.5G simulated sunlight illumination. (d) Photocurrent stability test of the champion CZTSSe photocathode at 0 V_{RHE} under illumination within 60 min.

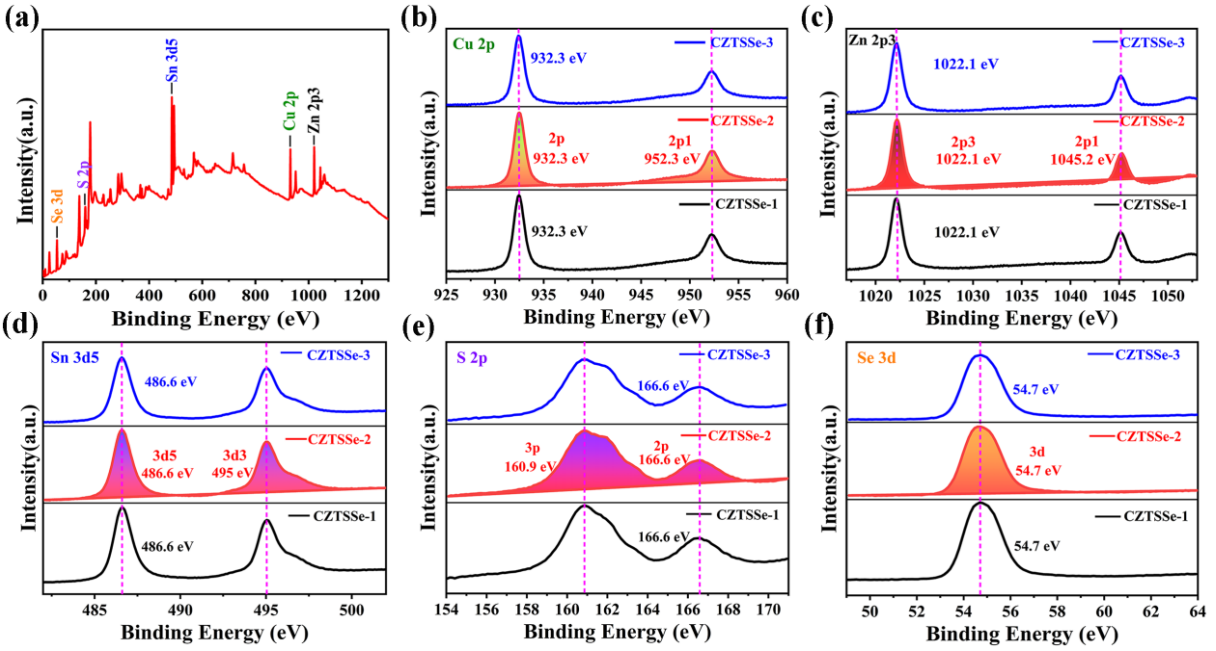

Figure S2. (a) Full scan XPS spectra of CZTSSe. (b) Cu 2p, (c) Zn 2p, (d) Sn 3d, (e) S 2p, and (f) Se 3d XPS spectra of CZTSSe thin films with different thicknesses.

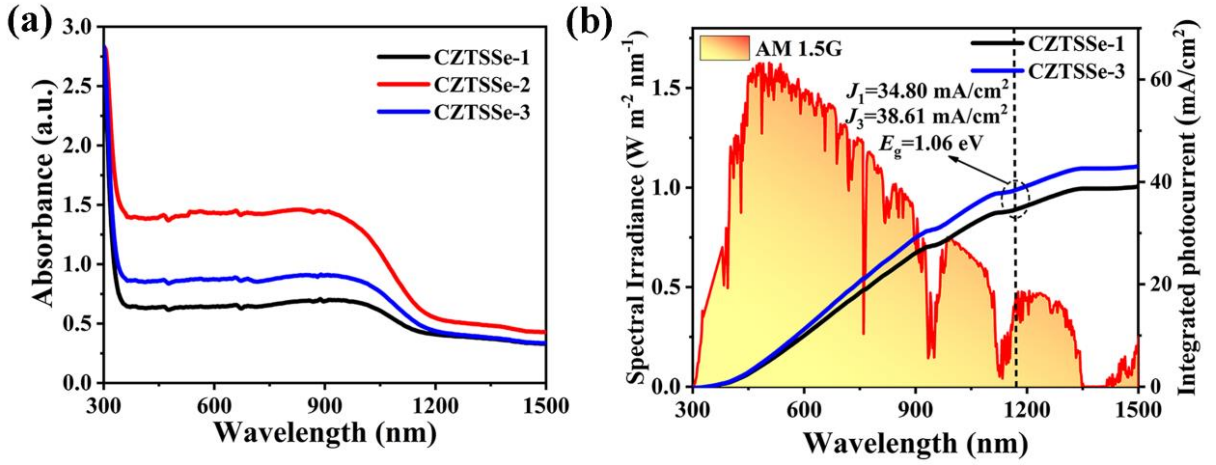

Figure S3. (a) Wavelength-dependent absorbance of the CZTSSe thin films with different thicknesses. (b) The energy density flux for the standard solar spectrum of AM 1.5G, and the integrated photocurrent density of the CZTSSe-1 and CZTSSe-3.

Table S2. Summary of the PEIS fitted parameters for the photocathodes.

Device	R_S(Ω)	R_{HF} (Ω)	C_{HF}(F)	R_{MF} (Ω)	C_{MF}(F)
PC-1	6.990	1.464	3.256×10^{-4}	24.69	1.236×10^{-3}
PC-2	6.673	0.7748	5.345×10^{-7}	4.127	1.488×10^{-3}
PC-3	6.588	2.851	7.177×10^{-5}	5.882	1.146×10^{-3}

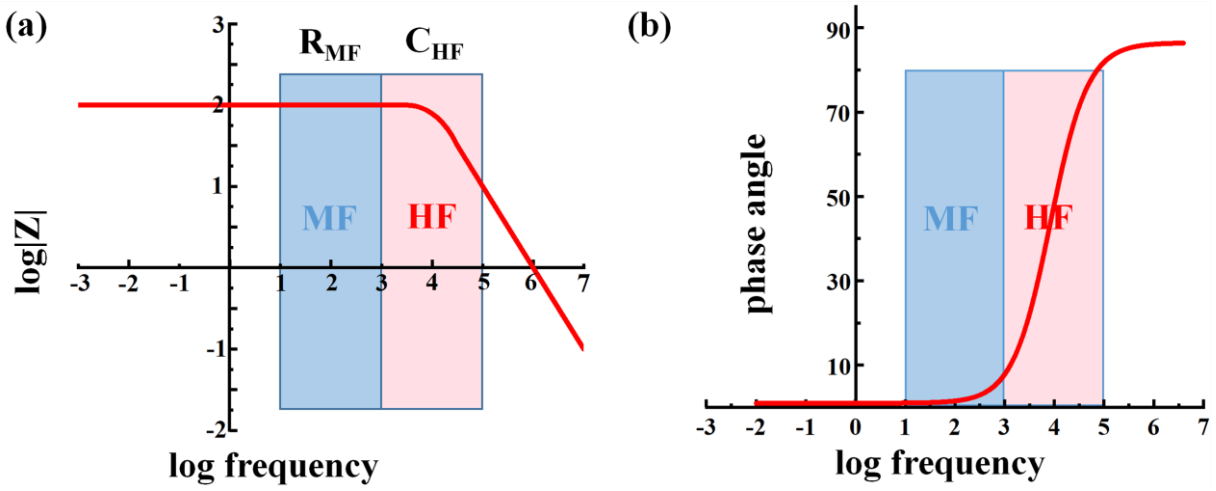

Figure S4. Diagrams of impedance (a), and phase angle (b) versus frequency in a parallel circuit.

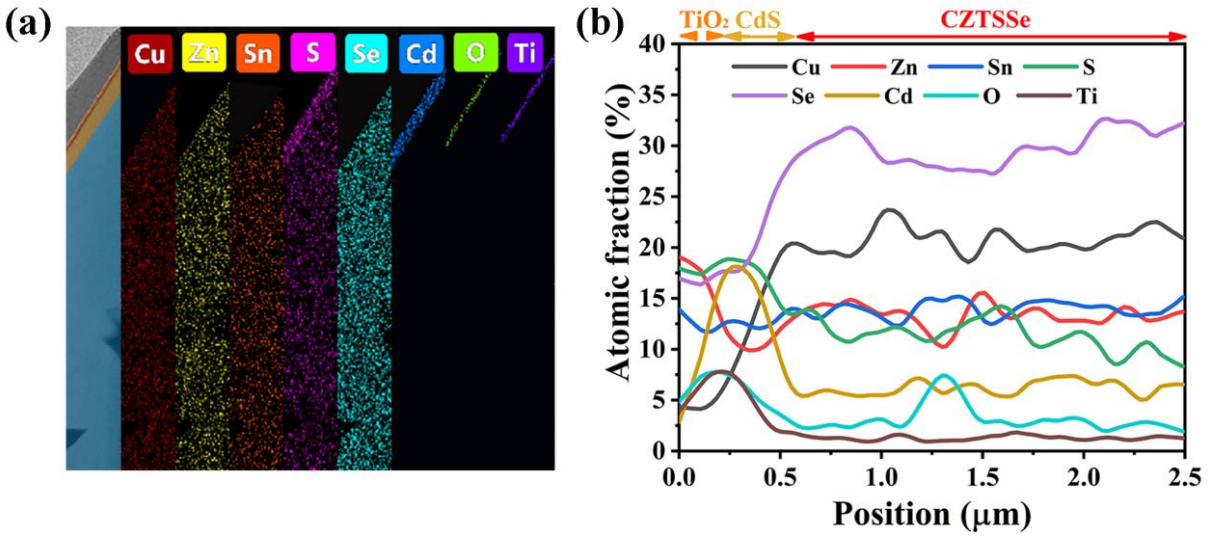

Figure S5. (a) TEM-coupled EDS elemental mappings of Cu, Zn, Sn, S, Se, Cd, O, Ti. (b) The corresponding EDS elemental line scan profiles.

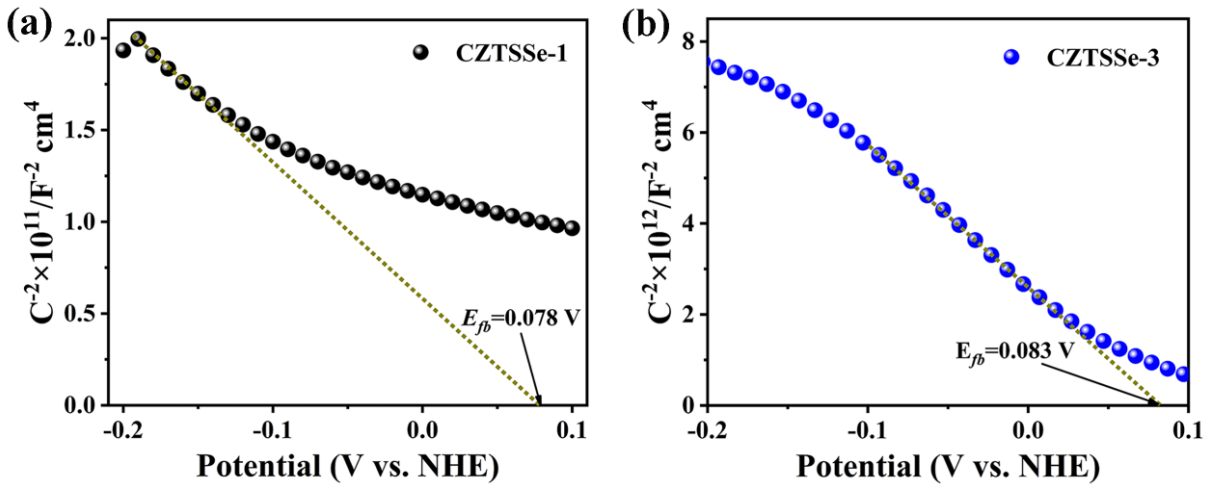

Figure S6. *M-S* plots of CZTSSe-1 (a), and CZTSSe-3 (b).

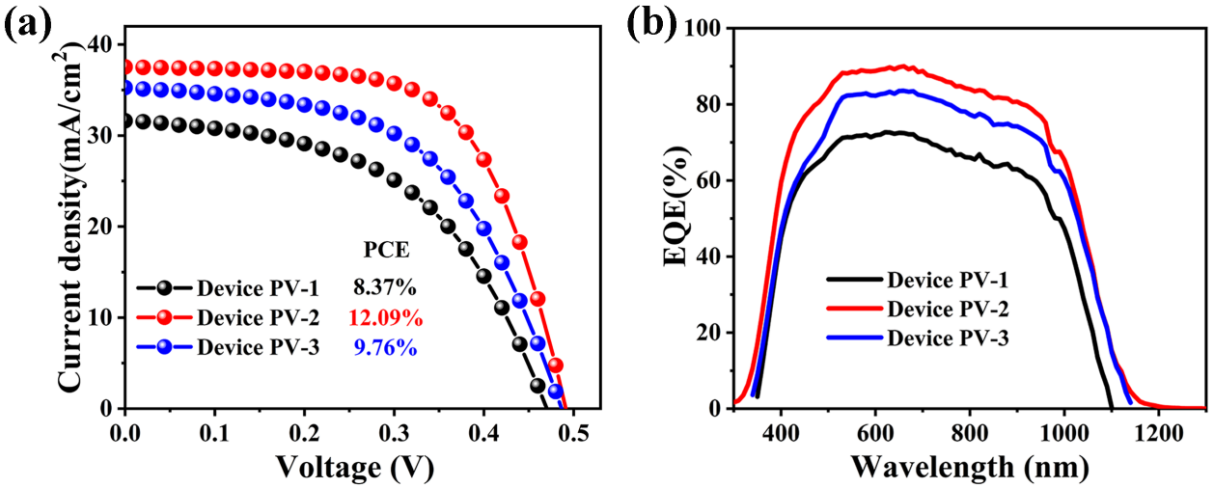

Figure S7. (a) *J*–*V* curves of the CZTSSe-based photovoltaic devices. (b) EQE spectra of the devices.

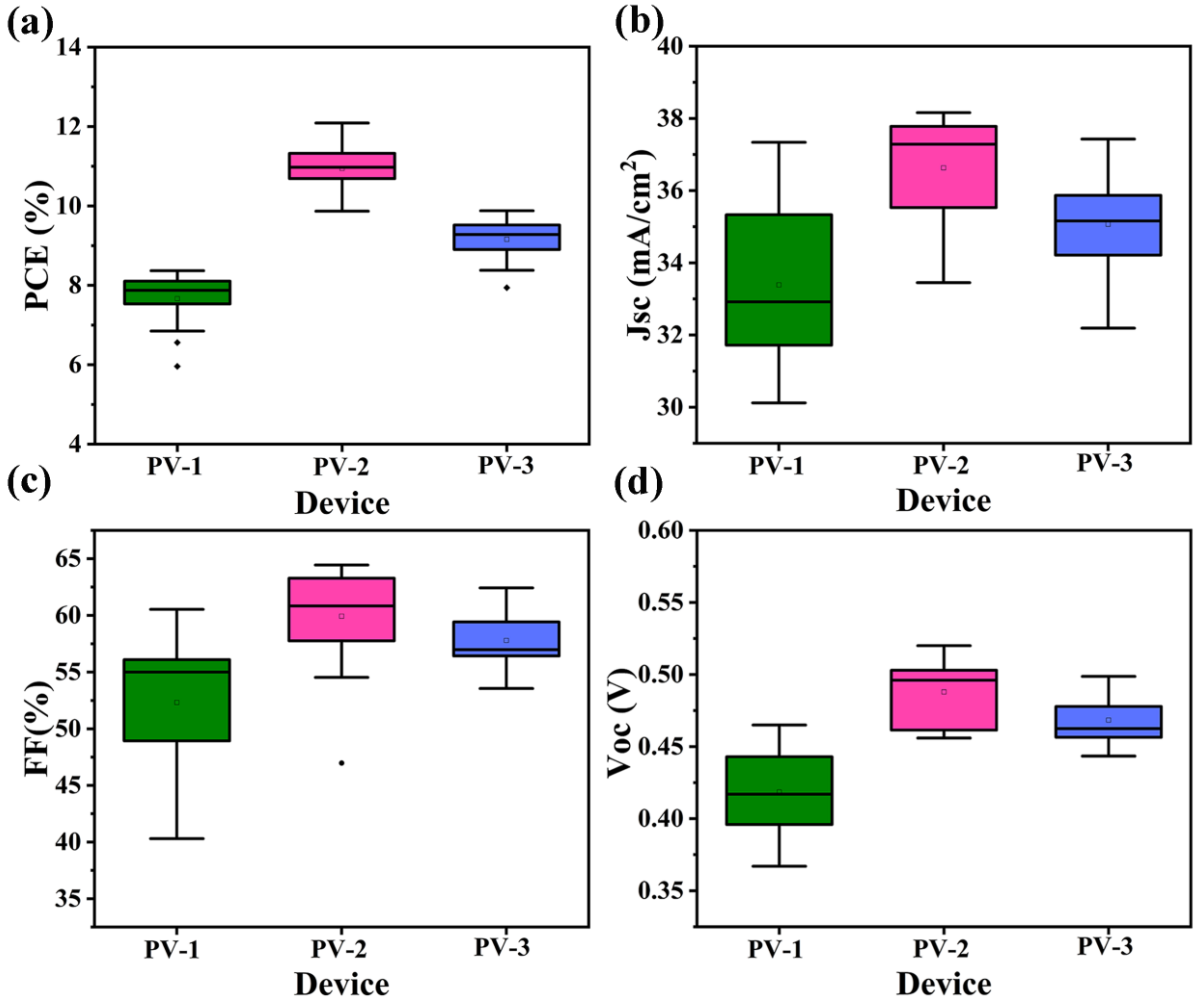

Figure S8. The statistical distribution of the CZTSSe-based photovoltaic device parameters, including (a) power conversion efficiency (PCE), (b) short-circuit current density (J_{SC}), (c) fill factor (FF), and (d) open-circuit voltage (V_{OC}).

Table S3. The representative CZTSSe-based photovoltaic device parameters.

Device	V_{OC} [V]	J_{SC} [mA cm^{-2}]	FF [%]	PCE [%]
PV-1	0.48	32.18	54.75	8.37
PV-2	0.50	38.18	63.33	12.09
PV-3	0.49	35.97	55.71	9.76

Table S4. Summary of the *C-V* and *DLCP* measurement results of the CZTSSe-based photovoltaic devices.

Device	N_{CV} (cm^{-3})	N_{DLCP} (cm^{-3})	N_i (cm^{-3})
PV-1	1.23×10^{16}	9.86×10^{15}	2.44×10^{15}
PV-2	1.66×10^{16}	1.53×10^{16}	1.30×10^{15}
PV-3	9.46×10^{15}	7.10×10^{15}	2.36×10^{15}

References

[1] M. Cao, X. Zhang, H. Gong, Y. Sun, S. Zhang, Y. Jiang, J. Zhang, Y. Shen, L. Wang, *Ceram. Int.* **2021**, 47, 25921-25931.

[2] J. Song, B. Teymur, Y. Zhou, E. Ngaboyamahina, D. B. Mitzi, *ACS Appl. Energy Mater.* **2021**, 4, 81-87.

[3] Y. Zhou, D. Shin, E. Ngaboyamahina, Q. Han, C. B. Parker, D. B. Mitzi, J. T. Glass, *ACS Energy Lett.* **2018**, 3, 177-183.

[4] D. Huang, K. Wang, L. Li, K. Feng, N. An, S. Ikeda, Y. Kuang, Y. Ng, F. Jiang, *Energy Environ. Sci.* **2021**, 14, 1480-1489.

[5] S. Grau, S. Giraldo, E. Saucedo, J. R. Morante, A. Llobet, C. Gimbert-Suriñach, *J. Mater. Chem. A* **2019**, 7, 24320-24327.

[6] C. Ros, T. Andreu, S. Giraldo, V. Izquierdo-Roca, E. Saucedo, J. R. Morante, *ACS Appl. Mater. Interfaces* **2018**, 10, 13425-13433.

[7] M. Chen, Y. Liu, C. Li, A. Li, X. Chang, W. Liu, Y. Sun, T. Wang, J. Gong, *Energy Environ. Sci.* **2018**, 11, 2025-2034.

[8] J. Zhao, T. Minegishi, H. Kaneko, G. Ma, M. Zhong, M. Nakabayashi, T. Hisatomi, M. Katayama, N. Shibata, T. Yamada, K. Domen, *Chem. Commun.,* **2019**, 55, 470-473.

[9] X. Wu, W. Zhao, Y. Hu, G. Xiao, H. Ni, S. Ikeda, Y. Ng, F. Jiang, *Adv. Sci.* **2022**, 9, 2204029.
[10] S. Chen, T. Liu, M. Chen, M. Ishaq, R. Tang, Z. Zheng, Z. Su, X. Li, X. Qiao, P. Fan, G. Liang, *Nano Energy* **2022**, 99, 107417.
[11] J. Su, T. Minegishi, K. Domen, *J. Mater. Chem. A* **2017**, 5, 13154-13160.